Science Advances
AAAS

Supplementary Materials for

Acoustofluidic tweezers via ring resonance

Xianchen Xu *et al.*

Corresponding author: Tony Jun Huang, tony.huang@duke.edu

Sci. Adv. **10**, eads2654 (2024)
DOI: 10.1126/sciadv.ads2654

This PDF file includes:

Other Supplementary Material for this manuscript includes the following:

Supplementary Text

Acoustic model of the ring resonance

1. Acoustic mode shape in the waveguide and ring resonator

To demonstrate the ring resonance in the designed acoustofluidic structure, we developed a theoretical model related to the ring resonance mode. As shown in Fig. S1, the wave propagation direction is perpendicular to the cross-section surface and along the *x* direction, where the width and height of the waveguide are *w* and *h*, respectively. We assume that the bottom of the PDMS waveguide is surrounded by air, the top is covered by water with height *d*, and the very top is the hard boundary. Thus, the governing equation for this system can be expressed as

$$\nabla^2 p_1(x,y,z,t) - \frac{1}{C_P^2}\frac{\partial^2 p_1(x,y,z,t)}{\partial t^2} = 0 \quad (1)$$

$$\nabla^2 p_2(x,y,z,t) - \frac{1}{C_0^2}\frac{\partial^2 p_2(x,y,z,t)}{\partial t^2} = 0 \quad (2)$$

Where ∇ is the Laplacian operator, C_P and C_0 are the wave speeds in the PDMS and water, respectively, and $p_{(1,2)}(x,y,z,t)$ is the acoustic pressure inside of the waveguide and water. Because the whole waveguide is made of PDMS, the model can be approached as a uniform waveguide. Then the elementary solution for the pressure can be written as

$$p_{(1,2),i}(x,y,z,t) = e^{j(\pm\beta x-\omega t)}\phi_i(y,z) \quad (3)$$

Where $\beta^2 = k^2 - \alpha_i^2$, $(\Re,\Im)\{\beta\} > 0$, and $k = \omega/C_{P,0}$, Here, α_i, $\phi_{1,i}$ are the eigen solutions of the transverse eigenproblem of

$$\nabla^2\phi_i = -\alpha_i^2\phi_{,i} \quad (4)$$

From Eqs.(1-4), the waveguide solution can be shown as a sum of these elementary solutions using the method of eigen mode expansion

$$p_{(1,2),i}(x,y,z,t) = \sum_{i\geq 1} e^{-j\beta x}\phi_i\,(y,z) \quad (5)$$

Where a_i and b_i are the coefficients determined as functions of the boundary conditions defined at the waveguide extremities. To solve the eigenproblems of Eq. (5), the boundary conditions between the interface of the waveguide and surrounding materials must be considered. Notably, the wave speed and mass density of air and PDMS are very different. The boundary condition

between the air and PDMS can be regarded as a soft boundary condition, the perturbation pressure is there, as is the acoustic potential.

Case 1: ① In the waveguide cavity $-h < z < 0$, the general solution from the boundary conditions can be written as a discrete sum of functions

$$\phi_1(y, -h < z < 0) = \sum_{n\geq 0}\{a_{1,n}\cos\left[k_{z1}(z)\right] + b_{1,n}\sin\left[k_{z1}(z)\right]\}\psi_n(y) \quad (6)$$

$$\text{With } \psi_n(y) = c_1\cos\left[k_{y1}(y)\right] + d_1\sin\left[k_{y1}(y)\right] \quad (7)$$

While at the boundary condition,

$$\phi = 0, \text{ if } z = -h \text{ and } |y| < w/2; \quad (8)$$

$$\phi = 0, \text{ if } y = \pm w/2 \text{ and } -h < z < 0; \quad (9)$$

With these boundary conditions, we have $\psi_n(y) = d_1\sin(k_{y1}y)$. Then, we have the wave number $\beta^2 + k_{z1}^2 + (n\pi/w)^2 = k^2 = \frac{\omega^2}{C_p^2}$, where, β^2, k_{z1}, and $n\pi/w$ are wave numbers in the x, z, and y directions. The solution will be

$$p_{1,i}(x, y, z, t) = \sum_{i\geq 1}\sum_{n\geq 0} e^{-j\beta x}\{a_{1,n}\cos[k_{z1}(z)] + b_{1,n}\sin\left[k_{z1}(z)\right]\}\psi_n(y) \quad (10)$$

The acoustic velocity in the PDMS can be expressed as $v_p = -\frac{1}{j\omega}\nabla p_{1,i}$, as we only consider the lowest order mode, i.e. *i*=1, n=0. $p_1(x, y, z, t) = e^{-j\beta x}\{A_1\cos[k_{z1}(z)] + B_1\sin[k_{z1}(z)]\}\sin(k_{y1}y)$

Case 2: ② in the water region, we arrive at a similar waveform

$$p_{2,i}(x, y, z, t) = e^{-j\beta x}\{a_2\cos[k_{z2}(z)] + b_2\sin\left[k_{z2}(z)\right]\}\psi_0(y) \quad (11)$$

At the bottom soft boundary,

$$\phi = 0, \text{ if } z = 0 \text{ and } |y| > w/2; \quad (12)$$

Which will make $a_2 = 0$ in Eq. (11). While, at the top hard boundary, $z = d$, $k_{z2}d = \left(\frac{1}{2} + n\right)\pi, n = 0,1,2$ ..., with the lowest order, $k_{z2} = \frac{\pi}{2d}$, For the solution in the water

$$p_{2,i}(x, y, z, t) = b_2 e^{-j\beta x}\sin\left[\frac{\pi}{2d}(z)\right]\psi_0(y) \quad \text{with} \quad \psi_0(y) = e^{-jk_{y2}y} \quad (13)$$

Since $\beta_{\square}^2 + k_{y2}^2 + (\frac{\pi}{2d})^2 = \frac{\omega^2}{C_0^2}$, k_{y2} can be the function of β, similarly, the velocity in this water region can be obtained by $v_0 = -\frac{1}{j\omega}\nabla p_{2,i}$. In region ④, it similar to the region ②, due to the symmetry of geometry, it has the solution in the water

$$p_{2,i}(x,y,z,t) = b_4 e^{-j\beta x}\sin[\frac{\pi}{2d}(z)]\psi_0(y) \quad \text{with} \qquad \psi_0(y) = e^{jk_{y4}y} \tag{14}$$

And the wave number $k_{y4} = k_{y2}$, due to geometric symmetry.

Case 3: ③ in the water region, we have the waveform

$$p_{2,i}(x,y,z,t) = e^{-j\beta x}\{a_3\cos[k_{z3}(z)] + b_3\sin[k_{z3}(z)]\}\psi_0(y) \tag{15}$$

With $\psi_n(y) = c_3\cos[k_{y3}(y)] + d_3\sin[k_{y3}(y)]$

For symmetric mode calculation, $b_3 = 0$. At the top hard boundary condition, $z = d$, $b_3 = \tan(k_{z3}d)a_3$.

Now, the unknown term is β, A_1, B_1, b_2, b_3, b_4, c_3, and d_3, we have the 3 internal boundary conditions,

$$\phi_1(y, z = 0) = \phi_3(y, z = 0) \tag{16}$$

$$\partial_z\phi_1(y, z = 0) = \partial_z\phi_3(y, z = 0) \tag{17}$$

$$\phi_2(y = -w/2, z) = \phi_3(y = -w/2, z) \tag{18}$$

$$\partial_z\phi_2(y = -w/2, z) = \partial_z\phi_3(y = -w/2, z) \tag{19}$$

$$\phi_4(y = w/2, z) = \phi_3(y = w/2, z) \tag{20}$$

$$\partial_z\phi_4(y = w/2, z) = \partial_z\phi_3(y = w/2, z) \tag{21}$$

Combined with condition Eqs. (8) and $b_3 = \tan(k_{z3}d)a_3$, the whole field is obtained. And as a result, the mode shape is also obtained. In the current study, only the first mode will be considered. Numerical simulation will be provided to get the mode shape, due to these functions are too difficult to compute analytically.

The ring resonator has a similar cross-section as the regular waveguide, but the shape is circular. As shown in Fig. S2, the ring resonator has the governing equation

$$\nabla^2 p_1(\boldsymbol{r}, z, t) - \frac{1}{C_w^2}\frac{\partial^2 p_1(\boldsymbol{r},z,t)}{\partial t^2} = 0 \tag{22}$$

The ring resonator also has a similar assumed solution to the regular waveguide,

$$p_{1,i}(\boldsymbol{r}, z, t) = \sum_{m\geq 1}\sum_{i\geq 1}(a_i e^{jk_{m,i}\boldsymbol{r}} + b_i e^{-jk_{m,i}\boldsymbol{r}})\phi_{m,i}\,(\boldsymbol{r}, z) \tag{23}$$

Here, we consider only the wave mode along the circumferential wave mode, since the designed width size of the structure is similar to the wavelength. This means the wave number of the resonance mode will be a function of the wavelength $k_{m,i} = f(\lambda)$. As discussed in the regular waveguide solution, the first mode shape (i = 1) lies along the cross-sectional direction (*y, z* direction), and the relation between the wavelength and wave number in the ring resonator can be expressed as

$$k_m = \frac{2\pi}{\lambda_m} \tag{24}$$

Where the wavelength and wave number also can be expressed as

$$\lambda_m = \frac{2\pi r_w}{m} \text{ with } (m = 1,2,3,\dots,N) \tag{25}$$

$$k_m = \frac{m}{r_w} \text{ with } (m = 1,2,3,\dots,N) \tag{26}$$

The wave speed of the ultrasound in the PDMS ring resonator is C_w, thus, the ring resonance mode frequency is given as

$$f_m = \frac{C_w m}{2\pi r_w} \text{ with } (m = 1,2,3,\dots,N) \tag{27}$$

As shown in Fig. S3, from equation (22), varying the radius and height will change the frequency of the ring resonance. As the radius increases, the resonant frequency decreases. With the same frequency, more eigenmode circle numbers need a larger radius, as shown in Fig. S3a with eigenmode circle mode m = 5, 10, 20, 50. The height also determines the mode shape of the eigenmode inside of the waveguide. As shown in Fig. S3b, h = 1 mm and 2 mm, the larger height tends to result in a higher order of eigenmode. In this paper, only the first order mode will be discussed and experimentally demonstrated.

2. Acoustic radiation force on particles in water

The radiation force on the particle is calculated semi-analytically. First, from both simulation and theory, we can obtain the acoustic field. Then for a specific particle, the Gor'kow potential field U can be calculated as

$$U = 2\pi R_P^3 \left(\frac{|p|^2}{3\rho_0 c_0^2} f_1 - \frac{\rho_0 |v|^2}{2} f_2\right) \quad (22)$$

Where $f_1 = 1 - \frac{\rho_0 c_0^2}{\rho_P c_P^2}$, $f_2 = \frac{2(\rho_P - \rho_0)}{2\rho_P + \rho_0}$, are constants that characterize monopole and dipole responses, respectively. The subscript *P* denotes the PDMS particles. The radiation force can then be estimated using $F = -\nabla U$. Here the Gorkov potential can provide a close approximation since the particle sizes are much smaller than the operating wavelength.

Simulation setup and additional simulation results

To maximize the acoustic intensity within the ring resonator, we investigated the effect of the gap. Fig. S4a illustrates a single-ring resonator positioned at the waveguide center, receiving an input signal with a resonant frequency of $f = 0.903\,MHz$ at port 1. The simulations were conducted using the acoustic-structure domain in COMSOL Multiphysics. Fig. S4b demonstrates that the normalized sound intensity varies with different gap sizes, reaching its peak when the gap measures approximately 0.2mm to 0.4mm, as highlighted in Fig. S4c. In this representation, the deep red color signifies the highest sound intensity.

To show the impact of thickness and validate the resilience of the ring resonance, we simulated a designed ring resonator with thicknesses of 1 mm (see Fig. S5a) and 4 mm (see Fig. S5b) using COMSOL Multiphysics. The results indicate that both designs exhibit a similar ring resonance response when subjected to identical inputs. This demonstration underscores the structural robustness of the design.

The designed ring resonator serves as an acoustic coding tool, guiding acoustic waves into specific patterns. Consequently, particles positioned atop the waveguide are patterned to reflect these distinct shapes, as illustrated in Fig. S6a and b. In this configuration, two ring resonators with varying depths are arranged in "L" and "+" shapes, allowing wave propagation along the coded shape when the input signal frequency matches the resonant frequency of the shape-coded

ring resonator. Consequently, the pattern's appearance and disappearance are dictated by different frequencies, showcased in Fig. S6c. The acoustic intensity on the resonated ring significantly surpasses that on the non-resonated ring for both "L" and "+" shapes, demonstrating notable variations in wave intensity as depicted in Fig. S6d and e. To validate the particle control capability, microscope images and simulated mode shapes are presented in Fig. S6f, confirming precise particle patterning aligned with the ring resonator's mode shape.

Experiment setup and additional experimental results

The experimental setup is shown in Fig. S9. Two lead zirconate titanate (PZT) transducers, measuring 15 mm by 20 mm by 2 mm and with a resonant frequency of 1 MHz, are employed as sources. In the first case, single-frequency waves are generated by both transducers using a function generator and then amplified by power amplifiers. The incident waves are focused and coupled into the waveguide through PDMS lenses (the detailed lens design is provided in Appendix B). The PDMS layer is tapered at both ends to enhance coupling into the guided mode. A standing wave pattern is established along the waveguide's path. During the experiment, the input voltage for both sources is set to 50 Vpp, consistent with previous literature. Upon activation of the source, the particles rapidly concentrate at the pressure antinodes. The ring resonator connected to the waveguide is in the center of the setup.

Fig. S10 shows the real experimental setup, where the microscope is located on the top of the structure and the water tank is filled with DI water. The structure is submerged inside the water tank.

Fig. S11 shows the fabricated PDMS particles whereas Fig. S11a shows the particles used in the experiment in PCR tubes and Supplementary Fig. 11b and c show the 50 μm red and blue PDMS particles under the microscope. The particle fabricated is approximately uniform.

To demonstrate the controllability of the ring resonance mode acoustofluidic tweezers, particles from 5 μm to 60 μm in diameter have been fabricated and tested using the two-ring ring resonance mode setup. As shown in Fig. S12, the mode shape can be obtained using the different sized particles at the ring resonator region and the image of PDMS particles under the microscope of varying sizes is also listed there. By changing the phase from φ_0 to $\varphi_0 + 2\Delta\varphi$, the particles with sizes from 20 μm to 40 μm will move along the ring path.

Fabrication process

This section describes all the fabrication processes of the experiment including the structure of ring resonance mode acoustofluidic tweezer in Fig. S15, ultrasound focus lens, and experimental test bed.

1. Fabrication process for the ring resonance acoustofluidic tweezers

All ring resonance mode acoustofluidic tweezers, including the multi-gates and multi-ports acoustic waveguide, are made with the same fabrication process shown in Fig. S16. ring resonance acoustofluidic tweezers device is fabricated with a standard process of curing PDMS on 3D-printed Molds. First, all casting molds were made by a 3D printer (Formlab 3B+) with clear resin (V4). This is followed by washing for 15 minutes in Form Wash, which contains Isopropyl Alcohol (VWR chemicals), and drying for 15 minutes in Form Cure. We highlight these two steps because it help to clean the surface impurities allowing easier peeling of the PDMS from the mold. Secondly, the PDMS base (Sylgard 184 Elastomer Kit, USA) and curing agent (Dow Corning, USA) were mixed with a ratio of 10: 1. The mixture is then degassed in a vacuum chamber for 30 mins to remove bubbles. At last, the liquid PDMS is poured into the 3D-printed ring resonance acoustofluidic tweezers mold and cured at 65°C for at least 2 hours. Next, the PDMS RRs acoustofluidic tweezers were peeled from the mold and shaped for experimental use. The ultrasound focus lens was fabricated by a similar process described above.

The PDMS with a base and curing ratio of 10 : 1, is then put inside of the mold and peeled from the mold after drying (see Figs. S17a-b). The simulation results (Figs. S17c-d) show that the designed focus lens will focus the acoustic waves at a single point or two points via a single-focus lens or a double-focus lens respectively. The two parts of the molds for the ultrasound focus lens are printed by a Formlab 3B+ 3D printer (see Fig. S17e). Fig. S18 shows a 3D simulation of the focus lens, where the acoustic focus point can be seen clearly in the center of the lens.

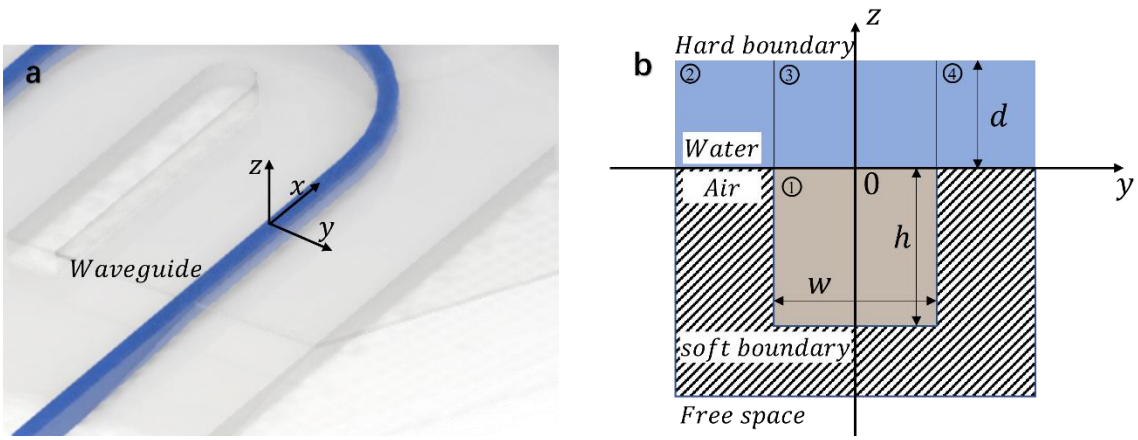

Fig. S1. Theoretical model of waveguide via acoustofluidics. **a**. A system consists of PDMS acoustic waveguides, shown in blue. **b**. The cross-section of the waveguide. The waveguide is located in the center and surrounded by water and air.

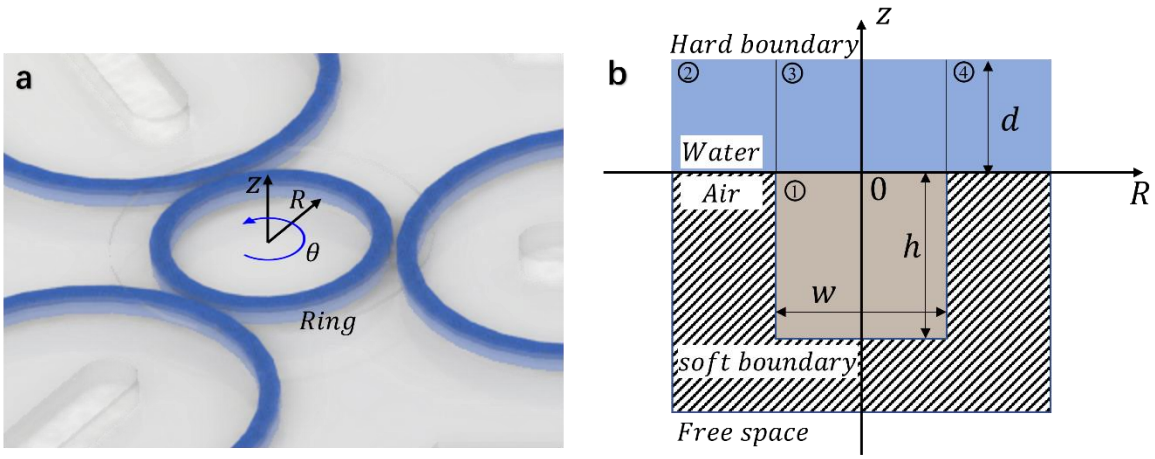

Fig. S2. Theoretical model of ring resonance via acoustofluidics. **a**. A system consists of a ring resonator and PDMS ring acoustic waveguides, shown in blue. **b**. The cross-section of the ring where the waveguide is located in the center and surrounded by water and air.

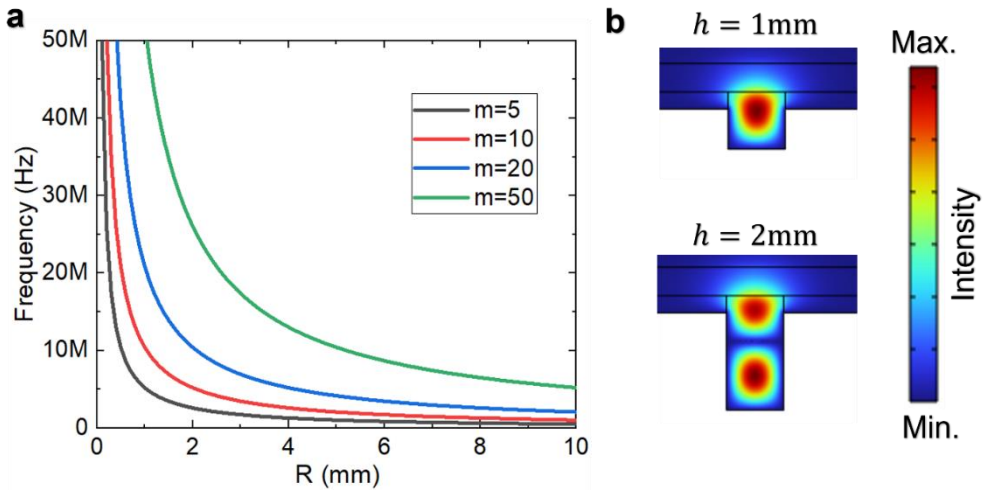

Fig. S3. Parameter discussion of ring resonance via acoustofluidics. **a.** Simulation results show the effect of changing the parameter *m* and varying the radius *R* of the PDMS acoustic ring waveguides on the frequency. The curves represent different values of *m* (5, 10, 20, and 50). **b.** Finite element method simulations depicting the mode shape of the waveguide with different heights. The color scale indicates the intensity of the acoustic field distribution within the waveguide.

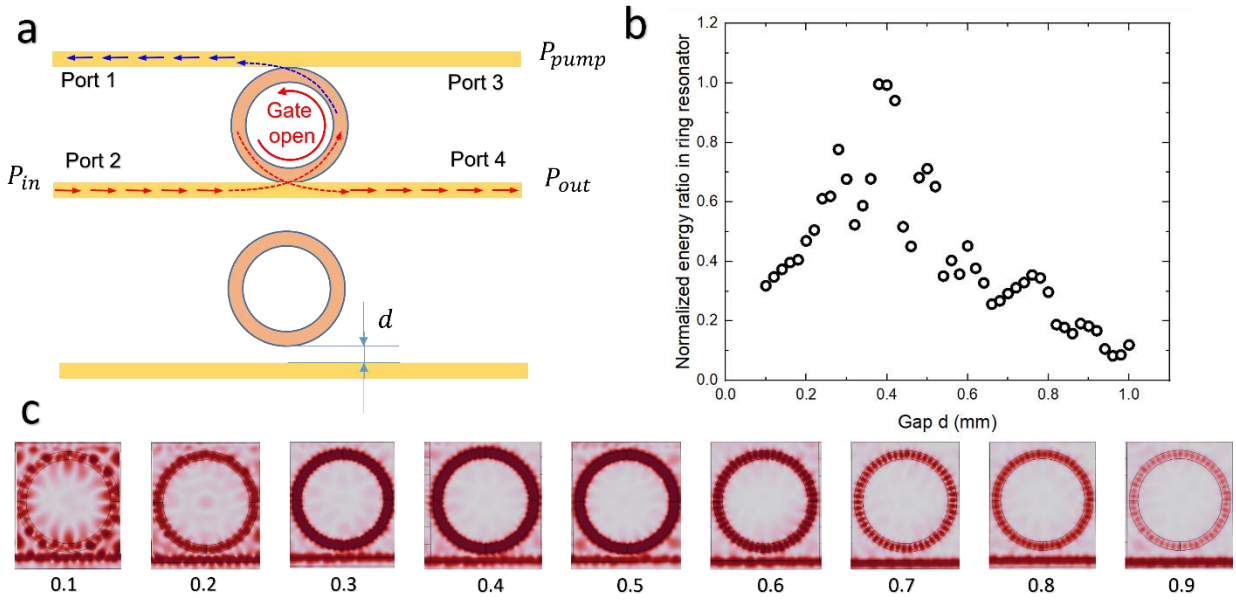

Fig. S4. The parameter study of the gap between ring-resonator and waveguide. **a.** Schematic diagram showing two waveguides placed on either side of the ring-resonator with the gap between the waveguide and ring-resonator denoted as *d*. **b.** Graph depicting the normalized acoustic intensity inside the ring resonator as the gap parameter *d* varies. **c.** Acoustic field distribution of the ring resonator and waveguide with gaps ranging from 0.1 mm to 0.9 mm. The series of images illustrate how the acoustic field distribution changes with varying gap sizes.

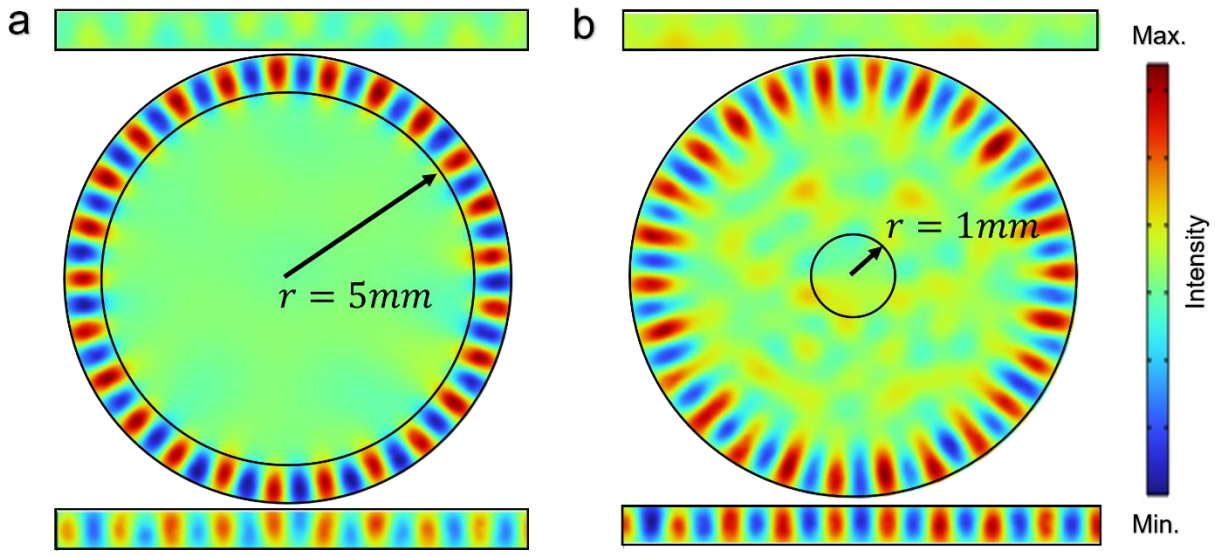

Fig. S5. Simulation result for ring resonance. a. ring resonance simulation with a ring resonator thickness of 1 mm and a radius of 5 mm, illustrating the resonant modes around the ring. **b.** Whispering Gallery Mode simulation with a ring resonator thickness of 4 mm and a radius of 1 mm, shows the change in resonant modes due to the increased thickness. The color scale represents the intensity of the acoustic field, highlighting the distribution of the resonant modes within the ring resonators.

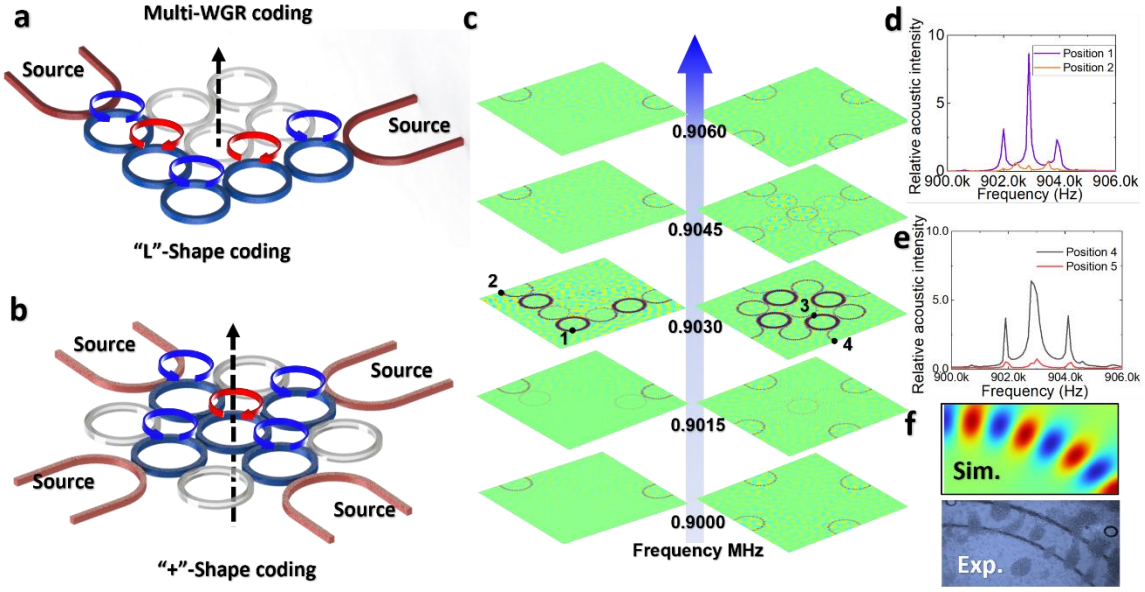

Fig. S6. Multi-Ring resonator coding the signal path via RR. **a.** and **b.** show the "L" shape and "+" shape coded by the ring resonator via R where the input source tries to create the resonate standing wave inside of the ring resonator respectively. The coding acoustic field distribution is shown in **c.** for the "L" and "+" shapes by varying the frequency from 0.9 MHz to 0.906 MHz, the resonance appears around 0.903 MHz. The corresponding relative acoustic intensity at Position 1 and 4 is shown in **d.** and **e.** respectively. In **f.** the ring resonance is simulated, and the control particle effect is also experimentally shown.

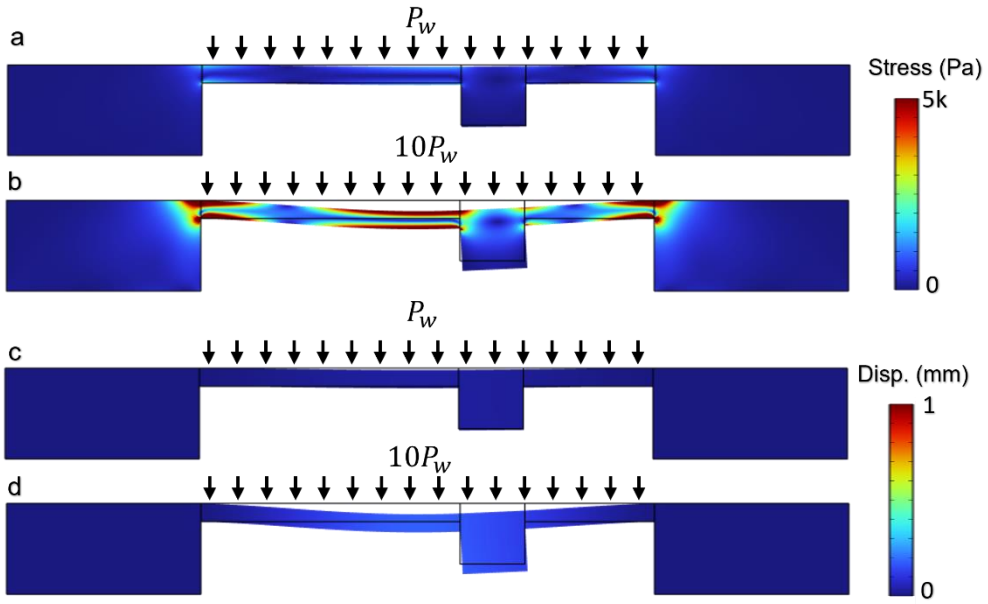

Fig. S7. Stress and displacement distribution with water. **a.** Stress distribution with water height of 0.5 mm. **b.** Stress distribution with water height increased tenfold. **c.** Displacement distribution with water height of 0.5 mm. **d.** Displacement distribution with water height increased tenfold. The color scale represents the magnitude of stress and displacement, illustrating the impact of varying water heights on the distribution patterns within the structure.

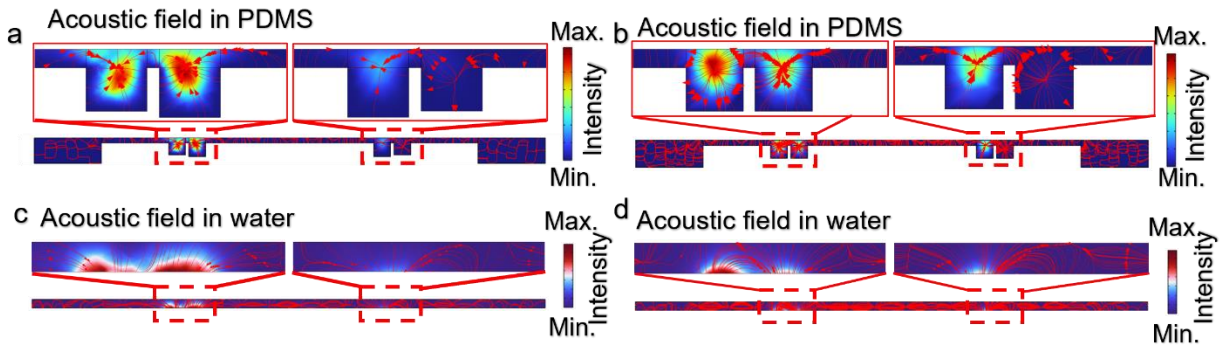

Fig. S8. Acoustic radiation field in PDMS and water. **a**. The acoustic field distribution in the cross-section of the waveguide and ring resonator, where the ring has a height of 1.1 mm. **b**. The acoustic field distribution in the cross-section of the waveguide and ring resonator, where the ring has a height of 1 mm. **c**. The acoustic field distribution in the water on top of the structure with a ring height of 1.1 mm. **d**. The acoustic field distribution in the water on top of the structure with a ring height of 1 mm. The color scale represents the intensity of the acoustic field, highlighting variations in acoustic pressure distribution within different structural configurations.

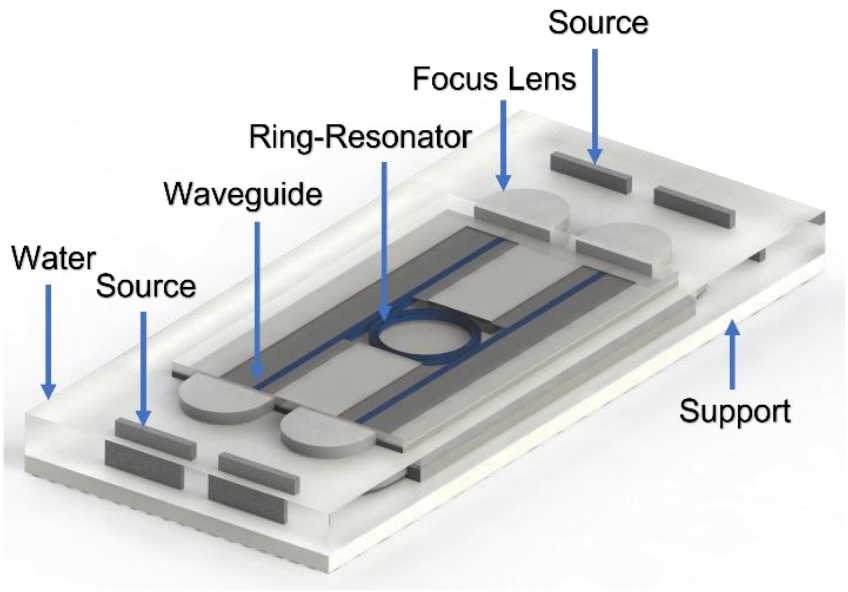

Fig. S9. Schematic of the experimental setup for ring resonance acoustofluidic tweezers. The diagram illustrates the key components, including the ring-resonator, waveguide, water source, and support structures. This setup is designed to facilitate the manipulation and control of particles within the acoustofluidic device, using the resonant properties of the ring-resonator and waveguides to achieve precise particle trapping and movement.

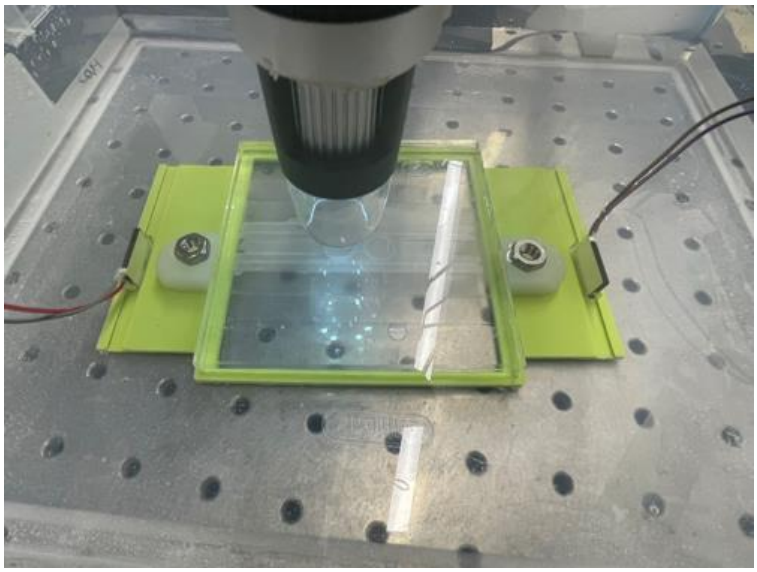

Fig. S10. Experimental setup of ring resonance acoustofluidic tweezers. The image shows the detailed arrangement used for the experiments, including the placement of the acoustofluidic device, the transducers, and the microscope for observation. The setup is designed to facilitate precise manipulation and visualization of particles within the acoustofluidic tweezers.

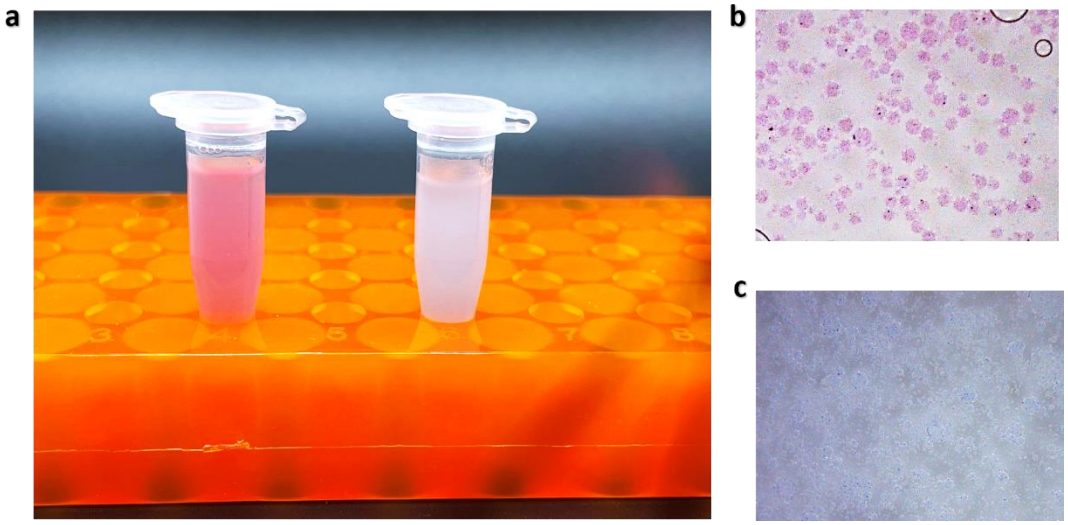

Fig. S11. The fabricated PDMS particles. **a**. The blue and red PDMS particles in PCR tubes. **b**. The 50 μm red PDMS particles were viewed under the microscope. **c**. The 50 μm blue PDMS particles were viewed under the microscope. The images demonstrate the distinct coloration and near uniform size of the fabricated particles, highlighting their potential for use in various experimental applications.

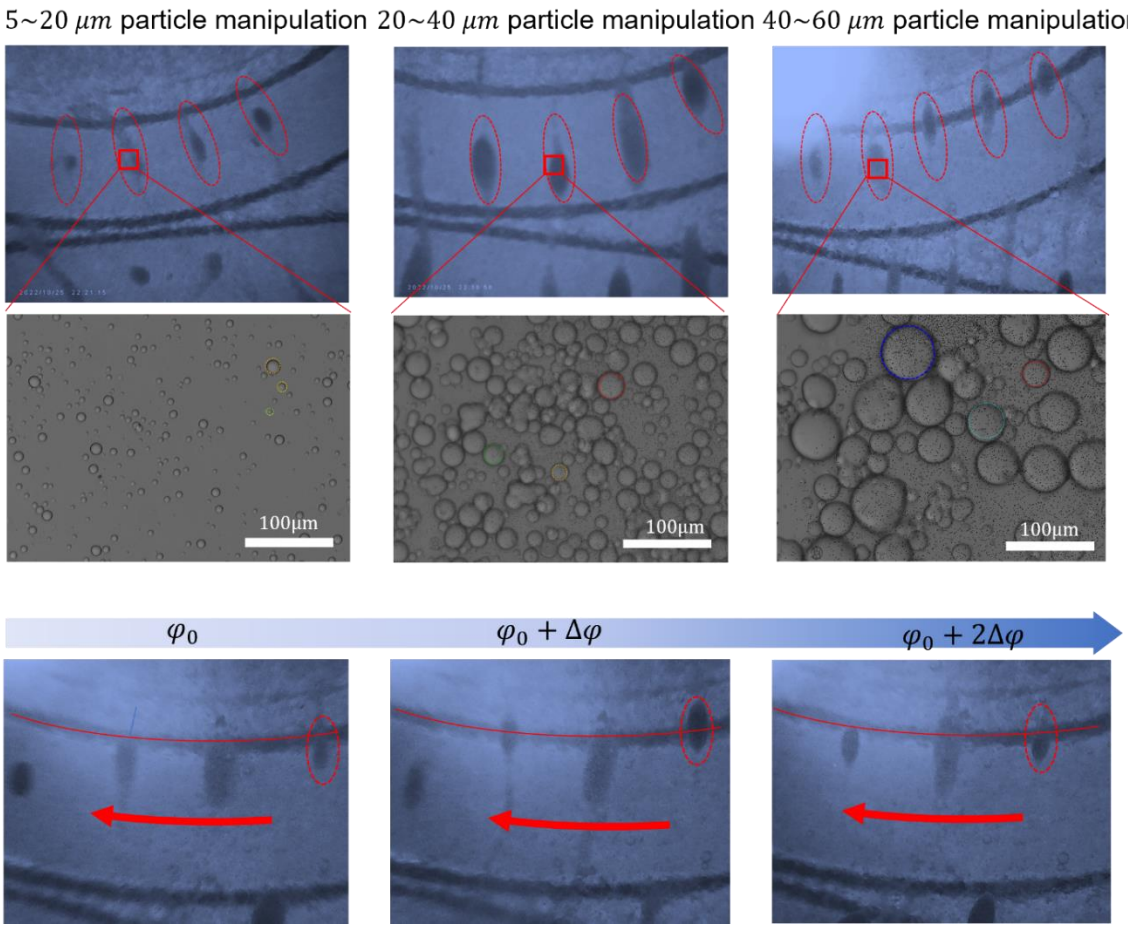

Fig. S12. Demonstration of particle manipulation ability via ring resonance acoustofluidic tweezers using PDMS particles of various sizes. The top row shows a sequence of images highlighting different regions (circled in red) within the experimental setup, with magnified views below each image displaying PDMS particles of different sizes. The bottom row illustrates the progression of particle movement as the phase of the input signal is adjusted (φ_0, φ_0+Δ φ, and φ_0+2Δ φ), indicated by the red arrows. Each magnified view includes a scale bar of 100 μm, demonstrating the precision of particle manipulation achieved through the acoustofluidic tweezers.

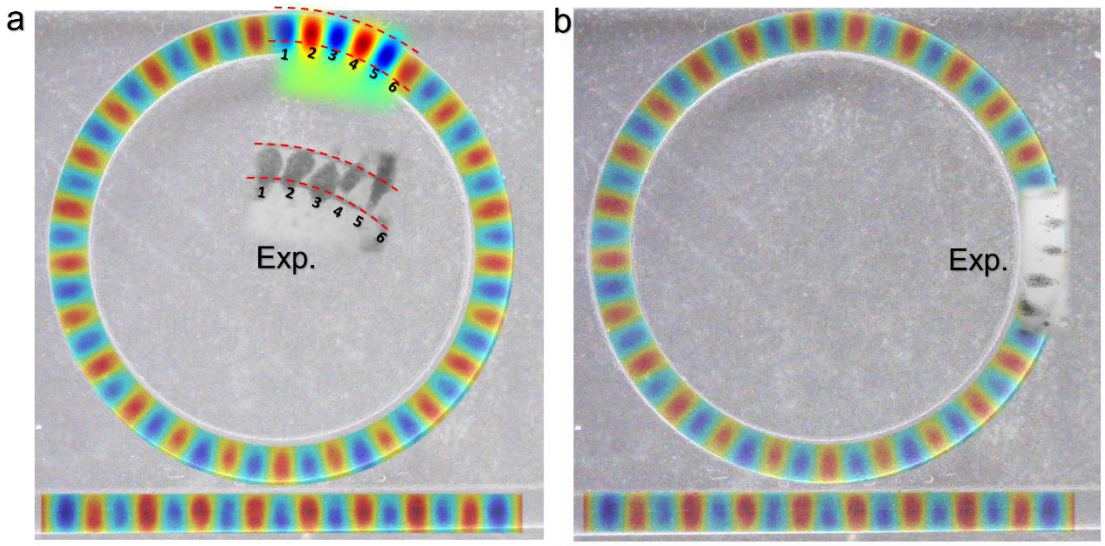

Fig. S13. Acoustic particles trapped on the ring resonator. The simulation illustrates the acoustic field within the waveguide and ring resonator, resulting from the acoustic radiation force within the standing wave field. This force leads to the trapping of particles within the ring, where they remain positioned at locations of maximal signal strength. **a**. PDMS particles were trapped near the top of the ring. **b**. PDMS particles were trapped near the middle of the ring.

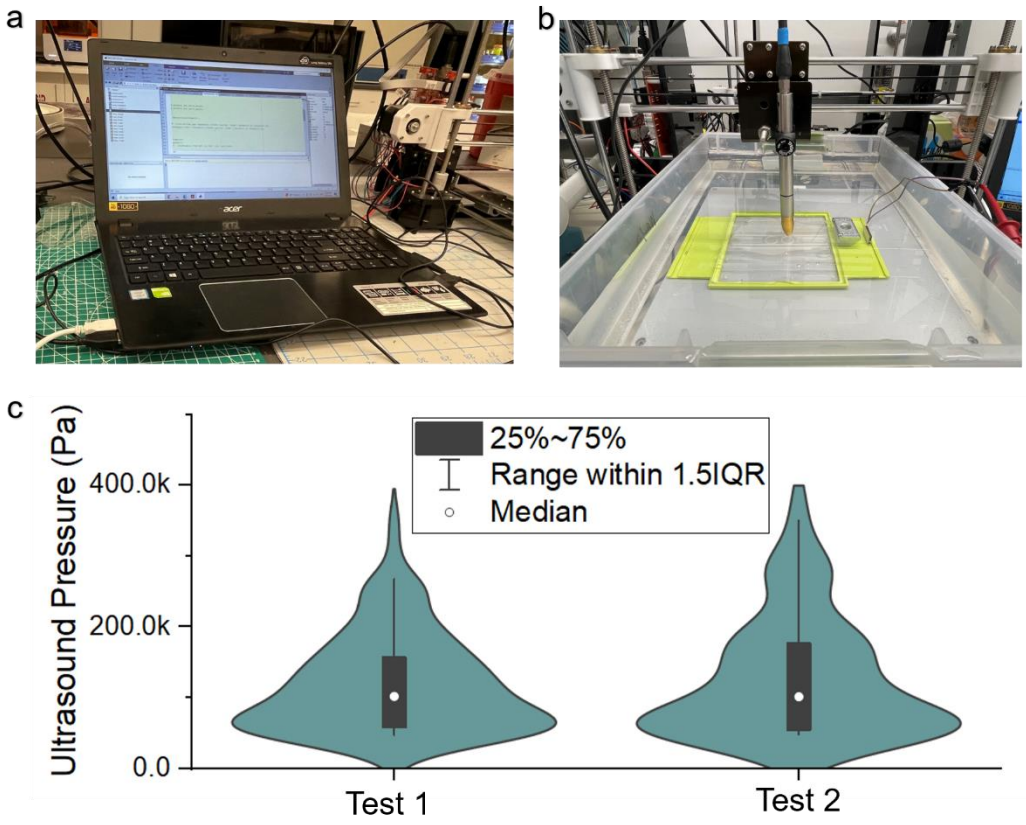

Fig. S14. Acoustic pressure measurement of ring resonator acoustofluidic tweezers. a. The image shows the control system of the measurement which will control the movement of the ultrasound ONDA hydrophone. **b**. The test bed is placed inside of a water tank, the ultrasound ONSA hydrophone is placed on the top of the test bed to measure the ultrasound pressure of the system. **c**. The experimental measurement shows the measured acoustic pressure on the top of the ring resonator. For both test 1 and test 2, the ultrasound pressure is in the safe region for human tissues and cells.

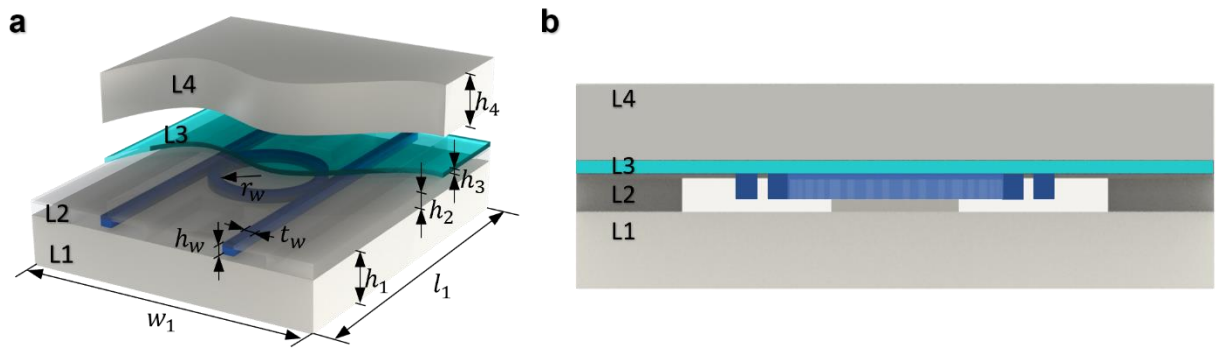

Fig. S15. The geometry details of ring resonance acoustofluidic tweezers in **a**. **b.** The cross-sectional view of the designed structure consists of L1: glass, L2: PDMS, L3: Water, and L4: Glass. The illustration provides a detailed view of how the layers are arranged and interact in the acoustofluidic tweezer setup.

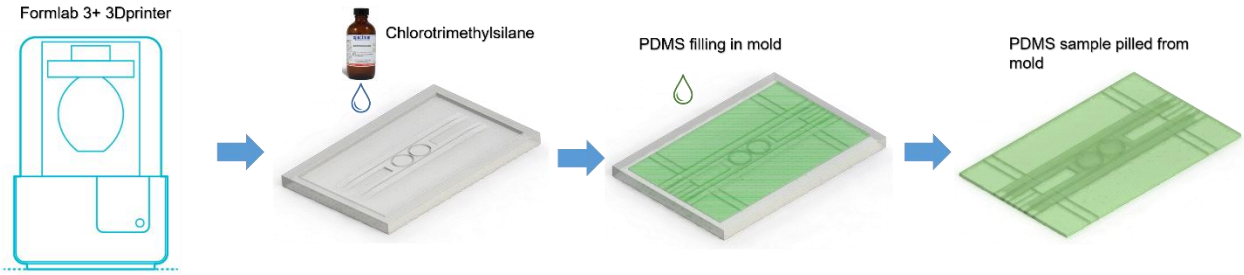

Fig. S16. Fabrication process of ring resonance acoustofluidic tweezers. The mold is printed using the Formlabs 3B+ 3D printer with clear resin. The structure is subsequently cast in polydimethylsiloxane (PDMS) to form the acoustofluidic tweezers. The images illustrate the step-by-step process from mold printing, resin pouring, and PDMS casting, to the final PDMS structure.

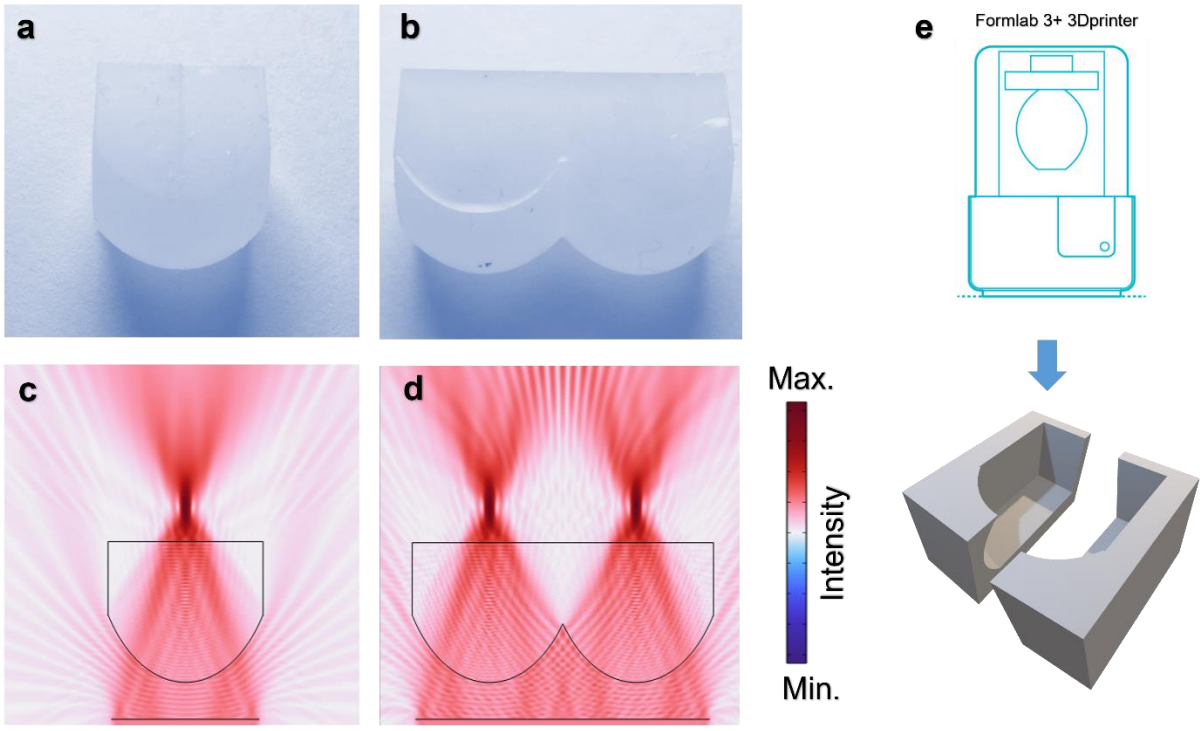

Fig. S17. Fabrication process and simulation results of focused lenses. **a.** The device shows the image of a single-focus lens made from polydimethylsiloxane (PDMS). **b.** The device shows the image of a double-focus lens also made from PDMS. **c.** Simulation of the acoustic field distribution for the single focus lens, showing the concentration of acoustic energy. **d.** Simulation of the acoustic field distribution for the double-focus lens, demonstrating the enhanced and divided focal regions. **e.** Diagram and 3D model of the mold used for fabricating the focus lenses via 3D printing.

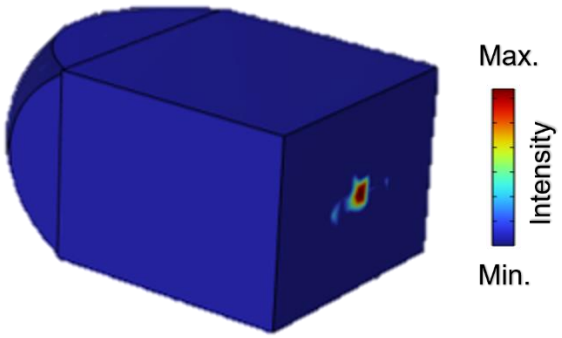

Fig. S18. 3D simulation of an acoustically focused lens. The simulation shows the spatial distribution of the acoustic pressure field, with the color scale representing the intensity of acoustic pressure—red indicating the highest intensity and blue indicating the lowest. The focused region of high intensity is visible near the right side of the simulation domain, demonstrating the lens's effectiveness in concentrating acoustic energy for precise manipulation of particles or cells. The dimensions are given in millimeters.

Table S1. Geometry and material parameters of the RR and waveguide. The geometric parameters of the proposed design are presented in this table, along with the material properties of PDMS, water, and glass used in the simulation.

Geometry parameters	Value	Materials parameters	Value
h_w	1 mm	*Density of PDMS*	970 kg/m^3
t_w	1 mm	*Sound speed in PDMS*	1040 m/s
r_w	5 mm	*Density of water*	1000 kg/m^3
h_1	10 mm	*Sound speed in water*	1500 m/s
h_2	1.5 mm	Density of glass	2500 kg/m^3
h_3	0.5 mm	*Sound speed in glass*	4540 m/s
h_4	10 mm		
w_1	100 mm		
l_1	100 mm		

Movie S1. The acoustic pressure distribution on the ring and waveguide. As the frequency approaches resonance, the acoustic pressure on the ring intensifies, reaching its peak at the resonant frequency. The waveguide facilitates the transmission of acoustic waves, while the ring experiences enhanced pressure due to resonance, showcasing the dynamic behavior of the system at this critical frequency.